行政院國家科學委員會專題研究計畫　期中進度報告

子計畫一：高性能、多工通訊晶片載具之設計與建構(1/3)

計畫類別：整合型計畫
計畫編號：NSC92-2220-E-009-006-
執行期間：92 年 08 月 01 日至 93 年 07 月 31 日
執行單位：國立交通大學電子工程學系

計畫主持人：鄭裕庭

報告類型：完整報告
報告附件：出席國際會議研究心得報告及發表論文
處理方式：本計畫涉及專利或其他智慧財產權，1 年後可公開查詢

中　華　民　國 93 年 5 月 26 日

行政院國家科學委員會補助專題研究計畫 成果報告 ■期中進度報告

用於寬頻通信之高性能單一載具整合晶片系統-子計畫一：高性能、多工通訊晶片載具之設計與建構(1/3)

計畫類別：■ 個別型計畫

計畫編號：NSC 92-2220-E-009-006-

執行期間： 92 年 8 月 1 日 至 93 年 7 月 31 日

計畫主持人：**國立交通大學電子工程系 鄭裕庭 助理教授**

共同主持人：

計畫參與人員：

成果報告類型(依經費核定清單規定繳交)：■精簡報告 □完整報告

本成果報告包括以下應繳交之附件：

□赴國外出差或研習心得報告一份

□赴大陸地區出差或研習心得報告一份

■出席國際學術會議心得報告及發表之論文各一份

□國際合作研究計畫國外研究報告書一份

處理方式：除產學合作研究計畫、提升產業技術及人才培育研究計畫、列管計畫及下列情形者外，得立即公開查詢

■涉及專利或其他智慧財產權，□一年□二年後可公開查詢

執行單位：**國立交通大學電子工程系**

中 華 民 國 93 年 5 月 31 日

高性能、多工通訊晶片載具之設計與建構(1/3)

Design and Fabrication of Si Carrier for RFSOP Applications

計劃編號: 92-2220-E-009-006- 執行期間:92 年 8 月~93 年 7 月

計劃主持人:交通大學電子系 鄭裕庭 助理教授 e-mail:ytcheng@mail.nctu.edu.tw

摘要

本計劃於第一年間成功開發出兩種致能技術，其分別為最佳化設計之高效能微機電式電感以及低溫鎳陶瓷奈米複合材料製程技術，本研究所開發之最佳化高效能微機電式電感，除了提供高達 40 以上之高品質因數的高頻訊號表現，更擁有較傳統微機電式電感之機械強度與穩定性，對於未來在整合載具之製作上提供具有高效能之高頻被動元件於電路設計者使用。而所開發之低溫鎳陶瓷奈米複合材料製程技術，發現 nickel-diamond 薄膜隨著嵌入於鎳金屬膜之鑽石粉末增加，將可增益楊氏系係數(Young’s Modulus)對密度比達 7 倍之多，此材料將可完全取代利用多晶矽膜之射頻微機電元件，本製程技術將可成功製作出超高頻之微振盪器之製作，將有助於下年度之整合載具之製作。倍之多，非常適合超高頻之微振盪器之製作。

ABSTRACT

Two enabling techniques have been successfully developed for the next stage of RF passive device fabrications in the following year, which are an optimum design and fabrication high *Q* RF inductor and low temperature nanocomposite synthesis for RFMEMS applications. An optimum micromachined spiral inductor is proposed and fabricated with fully CMOS compatible post-processes for RFIC applications. As compared, the new design of a 5nH micromachined inductor can have less 45% inductance variation than the conventional one while both devices operate at 8GHz but with 10 m/sec2 acceleration. Meanwhile, using a cross shape instead of blanket membrane can also effectively eliminate the inductance variation induced by the working temperature change (20°C to 75°C). Such inductors can have not only high Q performance but also better signal stability suitable for wide range RFIC applications. A low-temperature CMOS compatible stress-free electrolytic nickel (EL)/diamond nanocomposite synthesis has been developed and successfully utilized to fabricate cantilevers and electro-thermal microactuators to demonstrate the improvement of the device on reducing input power requirement and enhancing operation reliability. By calibrating the resonant frequencies of nickel cantilevers with different concentrations of diamond nanoparticles, the E/ρratio of cantilevers can be enhanced 7.1 times with diamond nanoparticles of 2 g/l in the proposed electrolytic nickel (EL) deposition process. From displacement tests, the electro-thermal microactuator with nanodiamond particles of 2 g/l can effectively reduce 73 % power requirement of pure nickel device needed at the same output displacement of 3 μm. It’s our belief that these two advanced techniques will facilitate our next step work in the three-year project.

INTRODUCTION

In order to achieve the proposed research work on the development of Silicon Integration Carrier (SIC) for RFSOP applications, several key techniques have been successfully developed in this year including high *Q* performance MEMS typed RF inductor, ultra low power microactuator, and CMOS compatible nanocomposite syntheses for high performance RF passive device fabrications. This report will introduce two major achievements in this project, which greatly enable our research work in the following year.

Recent progress in the design of personal wireless communication system is aimed for wide bandwidth applications [1,2]. In order to accomplish the goal, the RF carrier frequency of the system has to shift to 5~10 GHz range or even higher and low energy loss passive components such as inductor, capacitor, and transmission line, have to be implemented in the front-end RF circuitry for excellent signal integrity and low power consumption requirements. The on-chip micromachined spiral inductors are one of the “magic” components developed for [3,4] the purpose. Via the removal of the underneath silicon substrate, induced eddy current in the silicon substrate can be effectively prohibited that will result in the *Q* (quality factor) enhancement of the inductors while they operate at high frequency regime. Meanwhile, the parasitic shunt capacitance between the inductor and the substrate can be also reduced in terms of the mutual distance increase. Such a reduction can make the inductor resonant frequency towards higher value and suitable for itself in the high frequency operation.

However, the micromachined inductors also raise the mechanical reliability issues. Suspended structure of the inductors could suffer from the air pressure disturbance, mechanical thermal force disturbance or gravity disturbance [5-7]. Dahlmann and Yeatman [5] have investigated mechanically induced noise power effects onto the micromachined inductor and found that the noise should not be neglected and could be greater than the background thermal noise once the RF signal power levels above approximately 1mW. Since this type of the inductor is still with an emerging design, more studies must be done for its future applications. Thus, in this paper, we will further investigate the electric performance of the suspended inductor under accelerative and thermal stress disturbances and discuss the related influence to RF circuits using the contemporary simulation softwares, ANSYS and Ansoft-HFSS. Finally, based on the simulation results, an optimized micromachined inductor is proposed with a fully CMOS compatible post-process.

Metal-based micromachining technologies have attracted lots of attentions recently due to their superior material properities in certain applications, such as RF components and electro-thermal microactuators. For electro-thermal microactuators, lots of operating principles have been proposed, some of them used polysilicon as structural materials by silicon-based micromachining process [9,10], and some used metal as the structural materials [11,12].

Comparing with polysilicon, electro-thermally driven microactuators made of metal do not need doping process, are easier to achieve thicker structure by electroplating, and can provide larger output displacement with lower input voltage because of larger thermal expansion coefficient. However, the metal-based microstructure would suffer mechanical deficiency

such as fatigue and aging [13,14]. Also, it was found out that when operating temperature was higher than certain value, nickel structures would be degraded and an irreversible darkening on the device surface might occur [15]. Recent research in the nanocomposite synthesis, Teh et al. have proposed the incorporation of nanodiamond particles into an electroless nickel can greatly enhance the overall stiffness of nickel film due to the extreme hardness, stiffness, and temperature resistance of the diamond particle [16]. Besides, it was found that the higher the concentration of nanodiamonds being incorporated into the matrix, the less residual stress can exits in the composite film, which is very suitable for the fabrication of microactuators. In order to examine the possibility to employ the low-temperature stress-free electrolytic nickel (EL) nanocomposite deposition process for future MEMS device applications, .in this paper, the nanocomposite effects on the microactuators, cantilevers and electro-thermal microactuators, will be further investigated including effects on E/ρratio, power consumption, operating temperature, and reversible displacement range.

Part Ⅰ

- **DESIGN PROCEDURE OF THE MICROMACHINED INDUCTOR**

It is necessary to realize the mechanical disturbance effects for the optimum design of the micromachined inductor. In this study, a rectangular shaped spiral inductor with an air-bridge as shown in Fig. 1 is chosen since it has already been widely used in the RFICs. The underneath silicon substrate is removed using either wet or dry chemical etching processes to form the suspended structure. Under normal operation conditions, such inductors in the RFIC's for portable applications are generally susceptible with two kinds of environmental condition changes that are 10m/sec^2 (about 1G) acceleration change and 55°C working temperature variation (from R.T. to 75°C), respectively.

Regarding the mechanical deformation analysis of the suspended inductor caused by the changes, ANSYS simulator is utilized to monitor the inductor behavior. Solid/Thermal tetrahedron mesh is applied for the finite element analysis in the simulator based on the material properties as listed on Table 1. Once the deformation is determined by adding the gravity load or thermal stress on the device with suitable boundary conditions, the electrical model of the deformed spiral inductor is then built up in the HFSS simulator in terms of the nodal coordinates. The overall simulation procedure is described in Fig. 2.

Skin effect and substrate loss are two main factors to determine the outcome of an inductor performance. For the micromachined inductor, substrate loss mechanism is eliminated due to the high electrical resistivity of air. However, the skin depth of an inductor is inversely proportional to the square root of its driving frequency and material conductivity. In order to reduce the ohmic loss induced by the skin effect, the inductor thickness is generally designated larger than the skin depth. For instance, the skin depth of copper metal changes from 2.3 to 0.7μm while the driving frequency increases from 1 to 10GHz. Therefore, in this study, the inductors with two different kinds of thickness designs, 5 and 10μm, are chosen for the discussion in terms of their wideband applications.

A. Acceleration influence

The average simulated displacement variations (δ) in three dimensions of the inductors with 5μm thickness and 10um thickness, respectively, under 1G (~10 m/sec^2) acceleration along the direction of perpendicular to the inductor plane (z-direction) are summarized on Table 2, which are defined by the following relationship:

$$Avg(\delta) = \frac{1}{n}\sum_{j=1}^{n}(i_{afterdeformation} - i_{original}) \qquad (1)$$

where i is the coordinates of each node in the inductor. The nodal displacements in three directions are plotted in Fig. 3. According to the inductance variations simulated by HFSS for the two inductors, it is found the deformation of the inductors will result in the resonant frequency shift towards lower value as shown in Fig. 4. In addition, for the 1 to 10GHz applications, the inductor with thinner thickness will have less acceleration change influence as shown in Fig. 5.

B. Circuit influence

In RF frontend circuits, a lot of lumped inductors are required for the network matching purposes, such as the LNA and LC-tuned Voltage Controlled Oscillator. Especially to the VCO design, the oscillation frequency and phase noise described in equations (2) and (3) are strongly related to the inductance variation of the inductors (*dL/L*)[8]:

$$\omega_{oscillator} = \frac{1}{2\pi\sqrt{L_{inductor}\cdot C}} \qquad (2)$$

$$PN(\omega_m) = \frac{2kT\cdot R_{eff}\cdot F}{V^2{}_{amp}}\left(\frac{\omega_{oscillator}}{\omega_m}\right)^2 \qquad (3)$$

where $L_{inductor}$, C, $R_{effective}$, V_{amp}, ω_m, *and* F are the inductance of the rectangular spiral inductor, the capacitance of the resonator (mainly variable capacitance), parasitic resistance of the resonator, oscillation amplitude of VCO itself, the offset frequency from the center frequency and the noise figures of circuit, respectively. In general,

$$dPN(\omega_m)\,\alpha\,\frac{dL}{L^2} \qquad (3)$$

It indicates that phase noise variation can be up to 2dB difference @ 8GHz when a 10 thick micromachined inductor is used in a VCO circuit and suffered with 10m/sec^2 acceleration in which the inductance varies from 5.17 to 8.02nH. In addition to VCO, inductance variation could also cause the detrimental effects on the LNA performance due to the network impedance mismatches.

In order to resolve the reliability issue of the micromachined inductors, adding a dielectric membrane under the suspended structure is proposed to strengthen the inductors. According to Table 1, the Young's modulus of Si_3N_4 is 5 times higher than that of SiO_2. Though both dielectric materials have been widely used in CMOS circuitry, Si_3N_4 can have much higher residual stress with the underneath silicon substrate in comparison with SiO_2. Hence, we propose a sandwich ($SiO_2/Si_3N_4/SiO_2$) type membrane to compensate the stress issue but also to provide the mechanical support for the inductor. The membrane is consisted of 0.7μm thermal oxide, 0.7μm LPCVD Si_3N_4, and 0.7μm TEOS oxide. The double oxide layers can effectively release the membrane stress. According to the

simulation results as listed in Table 3, such a sandwich membrane can provide enough rigidity to the suspended inductor and make it less susceptible to the acceleration force.

C. Thermal stress influence

In general, the working temperature of a personal communication system could vary from 20 to 75°C or even higher due to the power dissipation of the device or surrounding temperature variation. Since the temperature change can deform the suspended inductor by the thermal stress originated from material's CTE (Coefficient of Thermal Expansion) mismatch, the structural enhancement via the incorporation of a dielectric membrane could create another reliability problem. According to the simulation results summarized in Table 4, 55°C temperature difference can deform the inductors with the blanket sandwich membrane support and the thicker inductor has more severe structure change.

■ ANALYSIS DISCUSSIONS AND OPTIMUM DESIGN OF THE MICROMACHINED INDUCTOR

Based on the previous investigation, the optimum design of the micromachined inductor has to rely on the success of the structural rigidity enhancement that can have less inductance variation while the device suffers the accelerative disturbance. Adding a dielectric supporting membrane might be a good method but it also leads to another reliability issue. In order to resolve the thermal stress influence without sacrificing the structure rigidity, a cross membrane structure as shown in Fig. 6 is devised for the optimization.

For 55°C working temperature change in the structure of the 5μm thick micromachined inductor with the cross shape sandwich dielectric membrane, the deformation along the x, y, and z-axes are 1.32E-02, 1.38E-02, and 3.84E-03(μm), respectively. Meanwhile, HFSS simulation shows that the cross-shaped membrane supported inductor can have 17% inductance variation less than the blanket one while they operate at 8GHz as shown in Fig. 7. The reduction of the inductance change is mainly attributed to the less deformation along the z-axis direction. In terms of the less physical constrains in the four corners of the inductor, which resulted in the deformation increase along the x/y direction, the deformation in the z-axis can be reduced so as to the inductance variation.

Part Ⅱ

■ CONCEPT DESIGN

The thermal microactuator used here is based on the long-short beam design [17]. The concept design is shown in Fig. 8, which consists of a pair of adjacent cantilever beams with different lengths, but the same material to form an actuating arm. By electrically resistive heating two beams, the tip of two beams curls toward the shorter beam due to the unequal thermal expansions of two beams. Here the length ratio of short beam to long beam is 0.5 with the long beam length of 800μm. The beam width is 10μm, and the gap between two beams is also 10μm.

■ FABRACTION PROCESS

In addition to the electro-thermal microactuators, cantilever beams with different amounts of diamond nanoparticles (0, 0.5, 1, and 2g/l) are first fabricated to identify the mechanical property enhancement. For the fabrication of the cantilever beams, as shown in Fig. 9, 1μm photoresist is first coated on the silicon wafer and patterned. Then thin Ti/Cu films (100Å/1000Å) are sputtered to act as the adhesion layer and seed layer, respectively, as shown in Fig. 9(b). The thickness of the seed layer is thin enough to reduce the internal stress without the seed layer ablation. Another 7μm photoresist is coated and patterned to act as the electroplating mold, as shown in Fig. 9(c). After that, the Ni or Ni-diamond nanocomposite films are electroplated at 50 ℃ to form the micro cantilevers, as shown in Fig. 9(d). Following are the sacrificial layer releasing with ACE (Acetone) and a rinse in deionized (DI) water as well as the air drying.

The fabrication process of the electro-thermal microactuators is similar, as shown in Fig. 10, except that 2μm HDP-CVD SiO_2 instead of the photoresist is deposited first on the wafer as the electrical isolation and sacrificial layers, as shown in Fig. 10(a). The wafer is immersed in diluted H_2SO_4 solution for 5 seconds to remove Cu seed layer. The Ti adhesion layer and SiO_2 isolation layer are removed in HF solution for 10 seconds.

■ RESULTS AND DISCUSSIONS

A. Surface morphology and elemental analysis

The morphology and surface elemental analysis of the cantilevrs are characterized by SEM and energy dispersive spectroscopy (EDS). Figure 11 shows the fabrication results of four cantilever beams made of pure nickel with beam width of 50μm, and beam lengths are 450μm, 350μm, 250μm, and 150μm, respectively. The distance between each beam is 50μm, and the thickness of the electroplating layer is 6μm. The device surface is very smooth. The EDS shown in Fig. 12 indicates that the electroplating layers contain little C. It may be resulted in the air stirring in the fabrication process.

The SEM photograph of fabricated four nickel-diamond cantilevers with the same dimensions as in Fig. 11 is shown in Fig. 13. The composition of electroplating layer is also identified by signature spectrums from EDS, where Ni-diamond nanocomposite films are found to contain C, O, Si, and Ni, as shown in Fig. 14. The diamond nanoparticles are found to be distributed uniformly in the electrolytic nickel film surface by EDS analysis at different points of the device with similar results.

One of the fabricated electro-thermal microactuators is, shown in Fig. 15, where the length of the long beam is 800μm, and the short one is 400μm. Beam width is 10μm, and the gap between two beams is also 10μm. The thickness of the device is 9μm. Indicators are also fabricated in front of the actuator tip for displacement calibration.

B. E/ρ ratio analysis

The Laser Doppler Anemometry (LDA) is used to calibrate variation of resonant frequency of cantilevers at different concentrations of diamond nanoparticles. The cantilever beam length is 350 μm and the width is 50μm. The thicknesses are 5.5μm (pure Ni), 5.08 μm (0.5g/l diamond), 5.06μm (1g/l diamond), and 4.4μm (2g/l diamond). Then, E/ρratio can be obtained by Eq. (1) [18]. The calibrated resonant frequencies are listed in Table 5, and the corresponding E/ρ values at different concentrations are plotted in Fig. 16. It is found that

the increasing diamond concentration can enhance E/ρratio evidently. For example, when concentration of diamond nanoparticles is 2g/l, the resonant frequency of the cantilever is about 2 times higher than the resonant frequency of the pure nickel beam with the same dimension, it means that E/ρ ratio of the Ni-diamond cantilever has been enhanced 7.1 times. Also, no crack is found in the surface of Ni-diamond film, which indicates that interfacial strength between nickel and diamond is good.

$$f = 0.1615\sqrt{E/\rho}\left(\frac{h}{L^2}\right) \qquad (1)$$

where

E **:** Young's modulus of the beam
ρ **:** the density of the beam
h **:** the thickness of the beam
L **:** the length of the beam

▪ DISPLACEMENT TESTS

In testing the electro-thermal microactuators, at the same output displacement of 3μm, the pure nickel device needs input power of 0.924W (V=2.1V, I=0.44A). With the increase of nanodiamond particles, the input power can be reduced. For example, at 2g/l, the Ni-diamond nanocomposite device only needs 0.248W (V=0.8V, I=0.31A), 73% smaller than pure nickel device power requirement, as shown in Fig. 17. Besides, the microactuator made of pure nickel would exhibit residual deformation once output displacement over 1.8μm (V=1.7V, I=0.37A), it means that the microactuator would not come back to initial position even the input power is removed. On the other hand, the microactuator made of Ni-diamond nanocomposite exhibits residual deformation only when output displacement is over 3μm. These results show that adding diamond nano particles in nickel electroplating the electro-thermal microactuator can effectively reduce the input power requirement, increase the reversible displacement range, and enhance the operation reliability.

▪ OPERATING TEMPERATURE OF ELECTRO-THERMAL MICROACTUATOR

The temperature of electro-thermal microactuator is measured by an infrared thermal microscope (Infrascope II, QFI). The microscope provides automated spatial emissivity compensation that produces a true temperature image of the tested device and computer controlled fine focusing stage. The specifications are listed in Table 6. The devices are tested on a stage with controlled temperature of 30°C. The measured maximum temperatures of electro-thermal microactuator under various applied voltages are shown in Fig. 18. In general, at temperatures higher than 350°C, nickel structures will be degraded and an irreversible darkening on the device surface may occur [15]. From experiments, the maximum temperatures of electro-thermal microactuators are all below 350°C at 0.4 DC volts.

▪ CONCLUSION

A new kind of micromachined inductor supported with a cross-shaped sandwich membrane has been successfully proposed. Two major simulators, ANSYS and Ansoft HFSS, are utilized for the optimum design and stability investigation of the micromachined inductors. Simulation results indicate mechanical disturbances like acceleration and thermal stress can easily cause conventional micromachined inductors with unstable performance that can be resolved using the new structural design. A low-temperature stress-free electrolytic nickel (EL) deposition process with uniformly dispersed diamond nanoparticles (diameter < 0.5μm) is proposed and successfully demonstrated here. The testing results show that the increasing diamond concentration can effectively enhance E/ρ ratio and reduce power requirement of electro-thermal microactuator to achieve the same output displacement. Furthermore, the reversible displacement range of microactuator is also found to be enlarged, which indicates the improvement on the device reliability by using Ni-diamond nanocomposite.

FIGURES AND TABLES

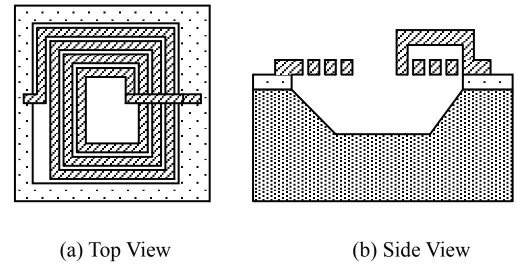

(a) Top View (b) Side View

Figure1. The layout of the micromachined inductors for the mechanical disturbances analysis (a) top view and (b) cross sectional view.

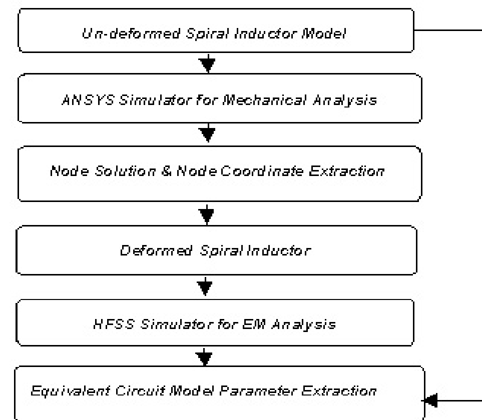

Figure 2. The process flow of the optimum design; the ANSYS simulator is utilized for the mechanical deformation analysis. Once the mechanical analysis is done, the new structural information is sent to the HFSS simulator for EM analysis.

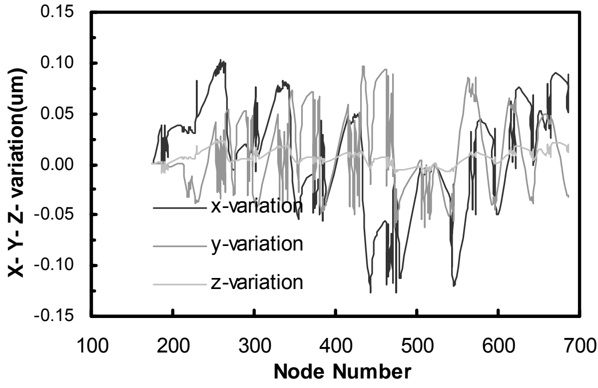

Figures 3. The nodal displacement of a 5um thickness inductor under 10m/sec^2 acceleration change.

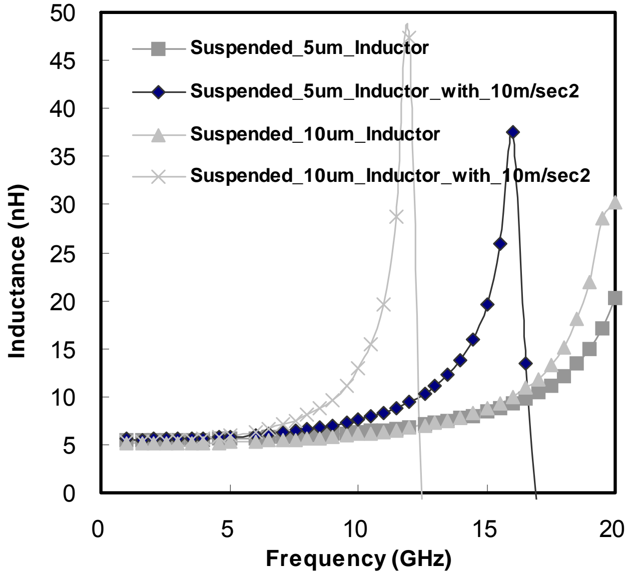

Figure 4. Comparison of the inductance variation between the original and that under the 10m/sec^2 acceleration change from 1 to 20GHz.

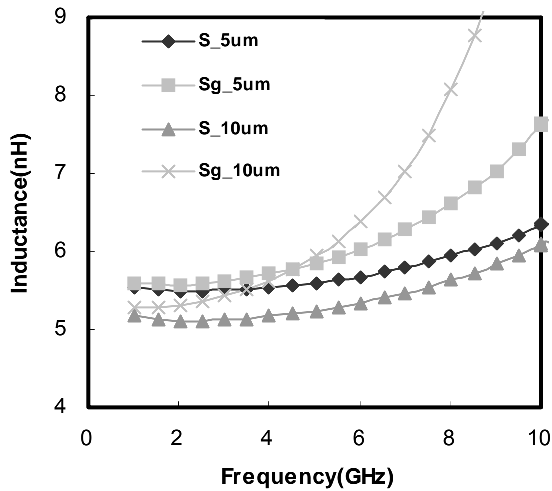

Figure 5. Enlarge view of the inductance variation between the original and that under the 10m/sec^2 acceleration change from 1 to 8GHz.

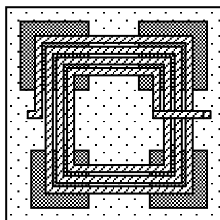

Figure 6. The layout of the cross shaped membrane type inductor.

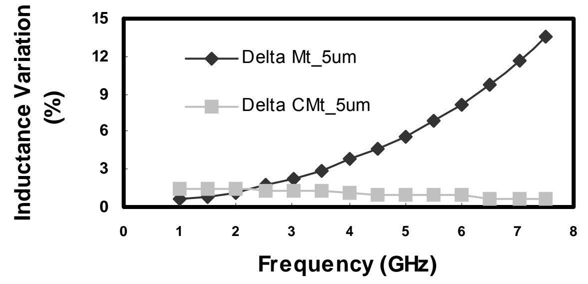

Figure 7. The inductance variation between the two 5μm thick 3.5 turns inductors both under 55° C temperature changes. Mt: the inductor supported with a blanket membrane. CMt: the inductor supported with a cross-shaped membrane.

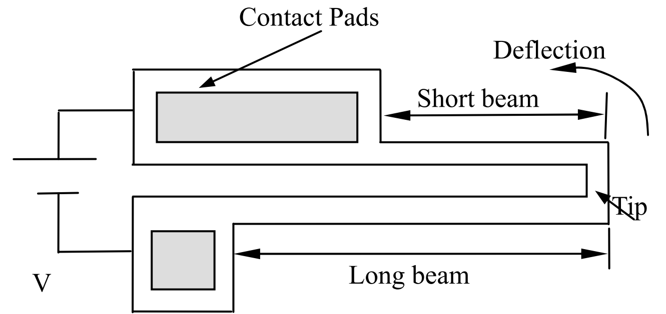

Fig. 8. The schematic diagram of the long-short-beam electro-thermal microactuator.[17]

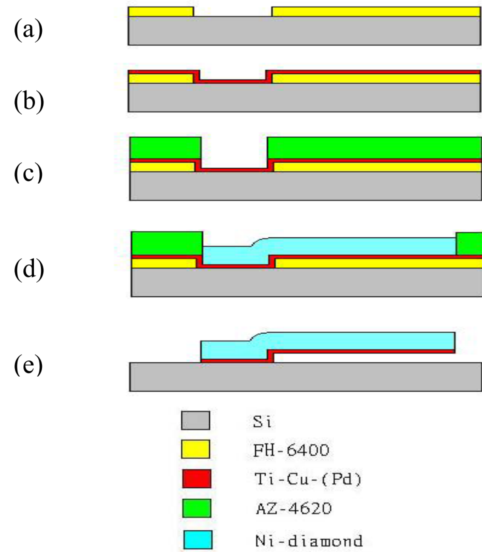

Fig. 9. Fabrication process of cantilever beam by metal-based surface micromachining process

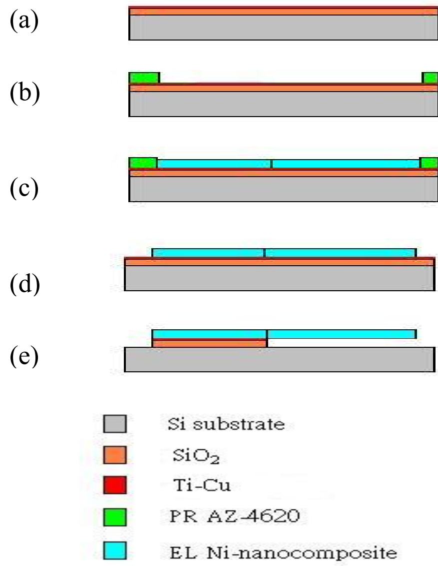

Fig. 10. Fabrication Process of electro-thermal microactuator by metal-based surface micromaching.

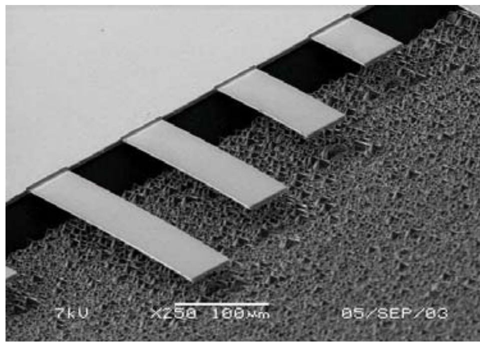

Fig.11. SEM of the fabricated electrolytic pure Ni cantilever beam.

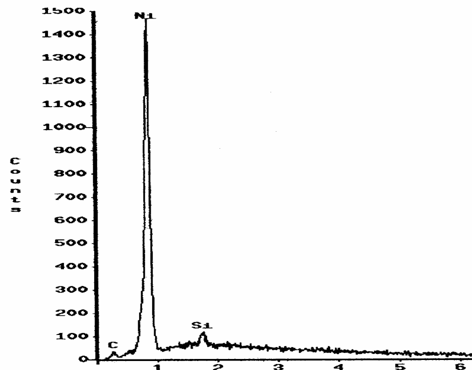

Fig. 12. EDS of the Electrolytic pure Ni.

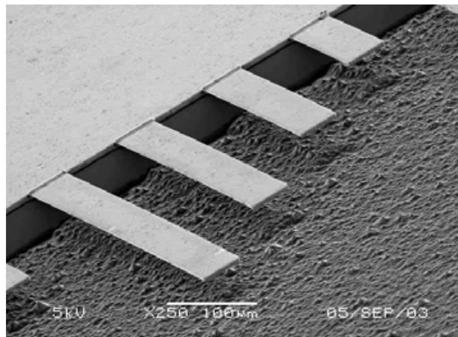

Fig. 13. SEM of the fabricated EL-diamond nanocomposite cantilever beam.

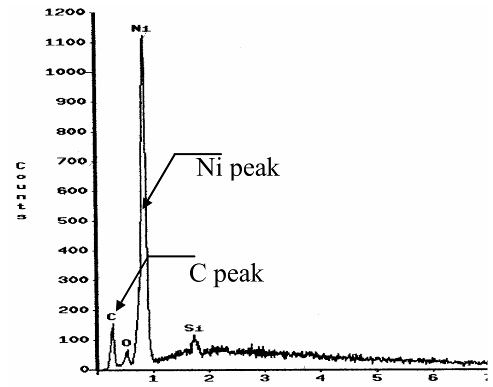

Fig. 14. EDS of nickel-diamond composite cantilever beam. The EDS show that diamond nanoparticles are well dispersed within the EL.

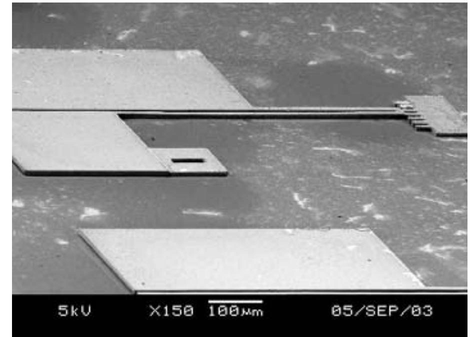

Fig. 15. SEM of the fabricated electro-thermal microactuator (Ni+2 g/L diamond nanoparticles).

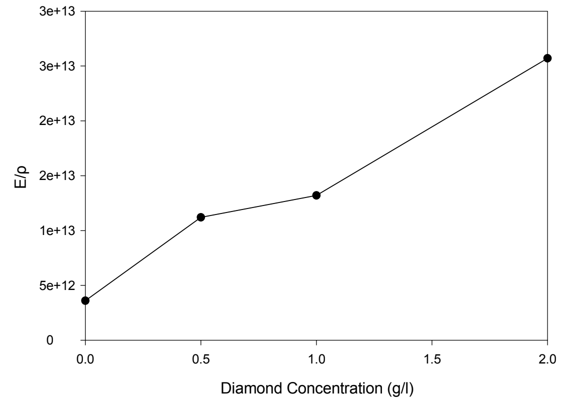

Fig. 16. The effect of the addition of various concentrations of nanodiamond into a nickel matrix is manifested in its E/ values.

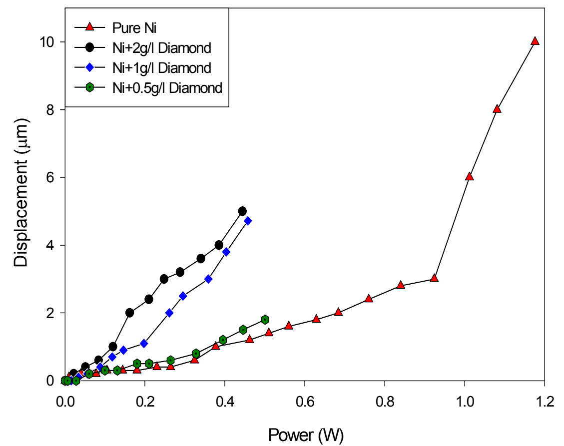

Fig. 17. Applied powers versus displacements of microactuators at different diamond nano particle concentrations.

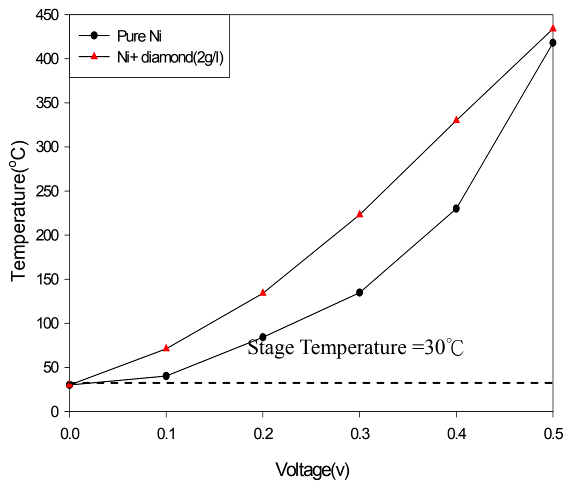

Fig. 18. The maximum temperature of microactuator (Ni+2 g/L diamond) under various applied voltages.

Table 1. The mechanical properties of the simulation materials.

Material	Cu	SiO_2	Si_3N_4
Thermal Expansion Coefficient (1/°C)	16e-6	5.5e-7	3.3e-6
Young's modulus (GPa)	125	73	310
Density (kg/m^3)	8900	2200	3290
Poisson Ratio	0.32	0.17	0.27

Table 2. Summary of the average displacement variations (μm) of the suspend inductors with 5um thickness and 10um thickness, respectively.

	x-direction	y-direction	z-direction
5um inductor (Sg_5um)	5.45E-02	3.96E-02	1.33E-02
10um inductor (Sg_10um)	5.91E-02	4.38E-02	1.18E-02

Table 3. Summary of the average displacement variations (μm) of the suspend inductors with a SiO_2/ Si_3N_4/ SiO_2 supporting membrane.

	x-direction	y-direction	z-direction
5um inductor (SMg_5um)	3.93E-03	3.56E-03	4.42E-03
10um inductor (SMg_10um)	5.28E-03	4.28E-03	7.56E-03

Table 4. Summary of the average displacement variations of the suspend inductors with blanket SiO_2/ Si_3N_4/ SiO_2 sandwich supporting membranes under 55°C working temperature change.

	x-direction	y-direction	z-direction
5um inductor (SMt_5um)	8.65E-03	7.83E-03	9.72E-03
10um inductor (SMt_10um)	1.16E-02	9.41E-03	1.66E-02

Table 5. The E/ρ values of various diamond nanoparticles concentrations in a nickel matrix.

Concentration of diamond nanoparticles (g/l)	Calibrated resonant frequency (KHz)
0	14.031
0.5	22.436
1	24.251
2	29.45

Table 6. Specification of the infrared thermal microscope

Specification	Description
Temperature Resolution	0.1℃
Temperature Range	30℃~800℃
Pixel Resolution	6 m(5X objective lens)
Spatial Resolution	12 m
Field of View (square)	1.54mm
Working Distance	52mm

■ Reference

[1] R. M. Schmalenberger and M. G. Edrich, “Channel modelling for wideband data communication in a maritime mobile environment”, Schmalenberger, IEEE/AFCEA EUROCOMM 2000 Information Systems for Enhanced Public Safety and Security., pp. 150-154, 2000.

[2] J. C. Adams, W. Gregorwich, L. Capots, and D. Liccardo, “Ultra wideband for navigation and communications”, IEEE Proceedings. Aerospace Conference, vol.2, pp. 785-792, 2001.

[3] H. Lakdawala, X. Zhu, X, H. Luo, S. Santhanam, L. R. Carley, and G. K. Fedder, “ Micromachined high-Q inductors in a 0.18-μm copper interconnect low-k dielectric CMOS process”, IEEE, JSSC, pp. 394-403, 2002.

[4] J. Hongrui, Y. Wang; J. –L. A. Yeh, and N.C Tien, ”On-chip spiral inductors suspended over deep copper-lined cavities” IEEE Microwave Theory and Techniques, pp. 2415-2423, 2000.

[5] G. W. Dahimann, and E. M. Yeatman; “Microwave characteristics of meander inductors fabricated by 3D self-assembly”, 8th IEEE International Symposium on High Performance Electron Devices for Microwave and Optoelectronic Applications, pp. 128-133, 2000.

[6] G. M. Rebeiz, “Phase-noise analysis of MEMS-based circuits and phase shifters”, IEEE Microwave Theory and Techniques, pp.1316-1323, 2002.

[7] D. J. Young, “Micromachined RF voltage-controlled oscillator with phase noise characterization” 9th International Conference on Electronics, Circuits and Systems, vol.1, pp. 295-298, 2002.

[8] J. Craninckx, and M.S.J. Steyaert, “A fully integrated CMOS DCS-1800 frequency synthesizer” IEEE, JSSC, vol. 33, pp. 2054 –2065, 1998.

[9] Linder, L. Paratte, M. A. Gretillat, V. P. Jaeckin and de N. F. Rooij, "Surface Micromachining", J. Micromech. Microeng., vol. 2, pp.122-132, 1992.

[10] M. E. McNie, R. R. Davies, N. Price, D. O. King, and K. M. Brunson, “Advanced micromechanical prototyping in polysilicon and SOI”, IEEE, 2000.

[11] Hsu, C. and Hsu, W., "Electrothermally-driven long stretch micro drive with monolithic cascaded actuation units in compact arrangement," Transducers'03, Boston, USA, June &-12, 2003.

[12] H. Guckel, J. Klein, T. Christenson, K. Skrobis, M. Landon, and E. G. Lovell,Thermo-Magnetic Metal Flexure Actuators Technical Digest, IEEE Solid State Sensor and Actuator Workshop, pp.73-75, 1992.

[13] H. C. Nathanson, R. A. Wickstrom, "A Resonant-Gate Silicon Surface Transistor With High-Q Band-Pass Properties", App. Phys. Letters, vol. 7, No. 4, pp. 84-86, 15 Aug. 1965.

[14] Long Que, Lisa Otradovec, Andrew D.Oliver , and Yogesh B.Gianchandani, "Pulse and DC Operation Lifetimes of Bent-Beam Electrothermal Actuators ",. The 14th IEEE International Conference on Micro Electro Mechanical Systems, pp. 570 –573, Jan 2001.

[15] L. Que, Park, J. S., and Gianchandani, Y. B., "Bent-beam electrothermal actuators—part 1: single beam and cascaded devices," J. Microelectromechanical systems, vol. 10, no. 2, pp-247-254, 2001.

[16] K. S., Y. T. Cheng, and L. W. Lin, " Nickel Nano-Composite Film For MEMS Applications ", The 12th International Conference on Solid State Sensors, Actuators and Microsystems, Boston, June 8-12, pp.1534-1537, 2003
[17] C. S. Pan and Wen Syang Hsu, "An Electro-thermally and Laterally Driven Polysilicon Microactuator", J. Micromech. and Microeng., vol. 7, pp.7-13, 1997.
[18] S. Timoshenko, D. H. Young, W. Weaver, Jr., Vibration Problems in Engineering, 4th Ed. New York: John Wiley and Sons, 1974.